

Sum-frequency generation in high-Q GaP

metasurfaces driven by leaky-wave guided modes

Rocio Camacho-Morales^{a,*}, Lei Xu^b, Haizhong Zhang^{c,**}, Son Tung Ha^c, Leonid Krivitsky^c, Arseniy I. Kuznetsov^c, Mohsen Rahmani^b, Dragomir Neshev^a

^aARC Centre of Excellence for Transformative Meta-Optical Systems (TMOS), Department of Electronic Materials Engineering, Research School of Physics, The Australian National University, Canberra, ACT 2601, Australia

^bAdvanced Optics and Photonics Laboratory, Department of Engineering, School of Science and Technology, Nottingham Trent University, Nottingham, NG11 8NS, UK

^cInstitute of Materials Research and Engineering, A*STAR (Agency for Science, Technology and Research), 2 Fusionopolis Way, #08-03, Innovis, Singapore 138634

KEYWORDS (Word Style “BG_Keywords”). Metasurfaces, GaP, nonlinear wave mixing, sum-frequency generation.

ABSTRACT. Resonant metasurfaces provide a unique platform for enhancing multi-wave nonlinear interactions. However, the difficulties over mode matching and material transparency place significant challenges in the enhancement of these multi-wave processes. Here we demonstrate efficient nonlinear sum-frequency generation (SFG) in multi-resonant GaP metasurfaces based on guided-wave bound-state in the continuum resonances. The excitation of the metasurface by two near-infrared input beams generates strong SFG in the visible spectrum, with a conversion efficiency of 2.5×10^{-4} [W⁻¹]. The measured forward SFG efficiency is two orders of magnitude higher than the one reported in Mie-type resonant metasurfaces. In addition, we

demonstrate the nontrivial polarization dependence on the SFG process. We show that in contrast to harmonic generation, the SFG process is enhanced when using **non-parallel polarized input-beams**. Importantly, by varying the input pump beam polarization it is possible to direct the SFG emission to different diffraction orders, thereby opening up new opportunities for nonlinear light sources and infrared to visible light conversion.

In the last few years, resonant dielectric metasurfaces have been used to study nonlinear optical processes, including harmonic generation and frequency mixing [1, 2]. **Dielectric metasurfaces based on GaAs [3-6] and Si [7-10] semiconductor materials** have been the prominent choice for enhancing second- and third-harmonic generation, respectively. **Alternatively, metasurfaces based on ZnO [11], TiO₂ [12] and Ge [13] have been used to study harmonic generation.** Since second-order nonlinear processes observed in non-centrosymmetric materials are intrinsically more efficient than their third-order counterparts [14, 15], there has been increased interest in exploring quadratic nonlinear metasurfaces. However, most second-order semiconductor materials have a narrow band gap, thus absorbing a significant portion of the nonlinear emission generated in the visible spectrum, or have a low second-order susceptibility. Recently, GaP has become an attractive alternative for studying nonlinear processes [16, 17], being a non-centrosymmetric material with high second-order susceptibility, high refractive index, and wider transparency range, compared to GaAs. Due to the advantages of this platform, GaP metasurfaces have been employed to study second harmonic generation (SHG) [18] and higher harmonic generation [19].

While resonant metasurfaces have been widely employed in the generation of harmonics, frequency-mixing processes remain largely unexplored. In harmonic generation processes the fundamental waves have the same properties, while in frequency-mixing processes such as SFG,

the excitation waves have different properties, including wavelength and polarization states [20]. The non-degenerate nature of frequency-mixing processes requires the design of multi-resonant metasurfaces and the engineering of the different participating modes [21-23]. Frequency-mixing processes can be useful for a number of applications including parametric oscillators [24], quantum information processing [25] and new frequency generation [26]. Here, we design and fabricate a double resonant GaP metasurface based on *waveguide-type* bound-state in the continuum (BIC) resonances. The fabricated metasurface is simultaneously illuminated by two waves at 875 nm and 1545 nm, generating a strong visible SFG at 558 nm. We reveal the nontrivial polarization dependence of the SFG, which required **non-parallel** input polarization states to maximize the conversion efficiency. We measure an SFG conversion efficiency of 2.5×10^{-4} [W⁻¹] in the forward direction, using a pump beam intensity of 137 MW/cm² and a signal beam intensity of 12.5 MW/cm². The observed efficiency is the highest SFG efficiency reported to date from thin metasurfaces.

In contrast to conventional local Mie-type resonances, bound states in the continuum (BIC) are collective resonances with non-decaying energy states, originally discussed in quantum mechanics by von Neumann and Wigner [27]. Due to the symmetry of such states, their radiation to free-space is forbidden, thus exhibiting an infinite quality factor. The signature of these ideal states can be experimentally observed near the BIC point, when a weak coupling to free-space radiation is possible, namely at the quasi-BIC condition. By controlling the free-space coupling, quasi-BIC modes can reach arbitrarily high-quality factors (high-Q) and strong field enhancements. Therefore, metasurfaces based on quasi-BIC resonances have been widely employed for enhancing harmonic generation [18, 28-31]. However, being lattice-type modes, the control of the mode-overlap and polarization properties becomes challenging for the SFG case.

To circumvent this issue, we employ leaky-wave BIC modes with broken translational symmetry imposed by two Mie-resonant nanodisks of different dimensions. The designed GaP metasurface simultaneously supports two narrow-band resonances at the wavelengths of the two input beams, termed here as pump (λ_p) and signal (λ_s) beams (Figure 1a), reflecting their input intensities. The unit cell of our metasurface consists of a long nano-waveguide adjacent to a pair of nanodisks, also known as nanodimer, each of them having a different radius (Figure 1a, dotted blue square). The nanobar width is 350 nm, and the radius of the two nanodisks is 150 nm and 120 nm (Figure 1b, inset). For more details on the geometrical parameters of our metasurface see Section 1 in the Supporting Information. **The guided modes of waveguides and photonic crystals have been previously investigated for nonlinear generation, due to their ability to highly confine and direct light [32-36]. However, some of the guided modes are totally bounded and cannot be directly excited using free space plane wave incidence (Figure S2, Supporting Information). Additional features are usually required to couple the external plane wave into these guided modes. To address this issue, we employ Mie nanodisk resonators to allow direct coupling of free-space incident plane waves into the guided modes, forming high-Q resonance metasurfaces.**

The calculated transmission spectrum of the metasurface, when illuminated by a y -polarized plane wave, is shown in Figure 1b. The spectrum exhibits two narrow resonances (gray-shaded regions) around the pump (λ_p) and signal (λ_s) wavelengths. When the metasurface is illuminated by an incident pump beam at λ_p , the excited multipolar resonances inside the nanodisks are dominated by an in-plane magnetic dipole, m_x . These multipolar resonances further couple the light into the highly confined mode TM(3,9,1) of the nano-waveguides. Meanwhile, when the metasurface is illuminated by an incident signal beam at λ_s , the generated hotspot in the gap of the nanodimer opens a leaky channel coupling the external light into the mode TE(2,1,1) and trapping the light in

the nano-waveguide. Similar to the Fabry-Perot model for leaky modes in optical resonant dielectric structures [37-39], we define here the modes $TE(l_x, l_y, l_z)/TM(l_x, l_y, l_z)$ with l_x, l_y, l_z corresponding to the number of peaks of the electric/magnetic field within the domain along x, y and z directions of the unit cell. The resonances at the wavelengths λ_p and λ_s have an estimated Q of 800 and 160, respectively, obtained numerically using an eigenmode solver (COMSOL). Figure 1c shows the calculated spatial distribution of the pump beam, where the electric field is strongly confined along the nano-waveguide and has a near-field enhancement of 30. Figure 1d shows the spatial distribution of the signal beam. In this case the electric field is partially confined along the nano-waveguide, with a near-field enhancement of 11, while lower field enhancement is observed in the boundaries of the nanodimer. The distribution of the fields, highly localized along the nano-waveguides, corroborates the excitation of the designed high-Q waveguide modes. Interestingly, the excitation of Mie resonances (in the nanodimers) and guided modes (in the nano-waveguides) correlates to the excitation of BIC modes in metasurfaces. This correlation is supported by the multipolar analysis of mode TE (2,1,1), included in Figure S3 of the Supporting Information.

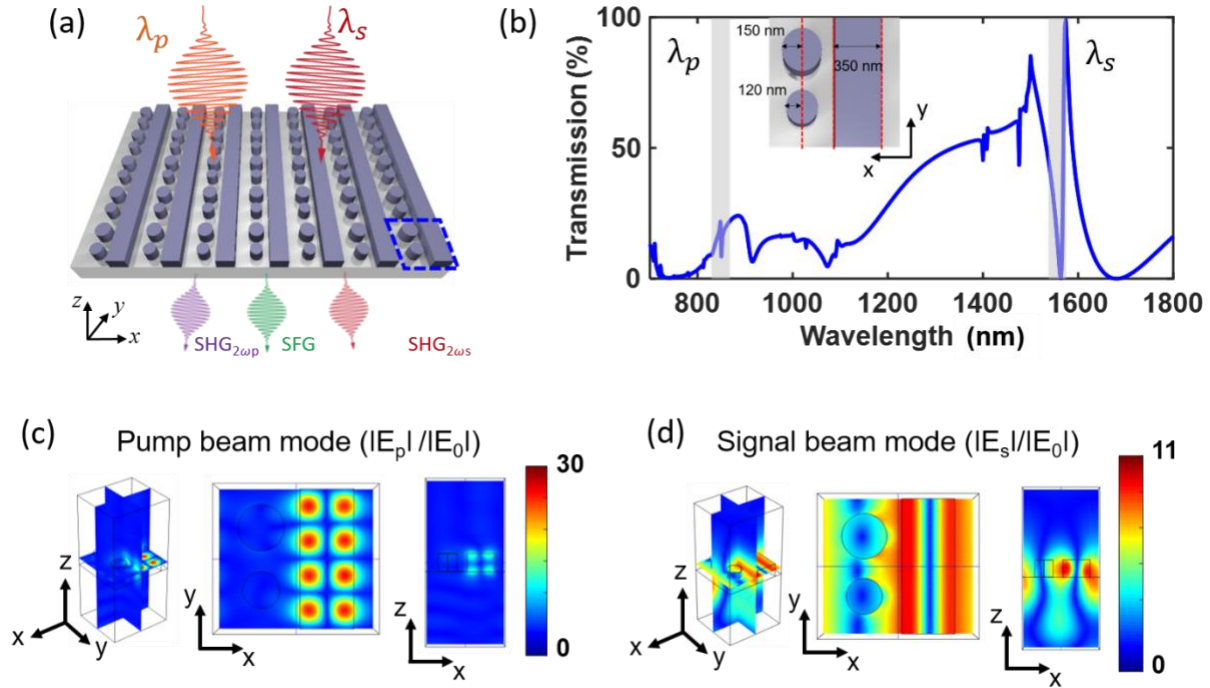


Figure 1. (a) Schematic of designed GaP metasurface, simultaneously illuminated by pump (λ_p) and signal (λ_s) beams to generate several nonlinear emissions. The unit cell of the metasurface is indicated by a dotted blue square. (b) Calculated linear transmission of metasurface considering an incident y -polarized plane wave. The transmission spectrum exhibits two sharp resonances around the pump and signal wavelengths, indicated by gray vertical bars. Inset: geometrical dimensions of the metasurface unit cell. Calculated modulus of the electric field distribution in a metasurface unit cell for the incident (c) pump beam and (d) signal beam. The field intensity in both plots is represented by the side color bars.

We fabricated monocrystalline GaP metasurfaces according to our design, using electron beam lithography followed by reactive ion etching. For details of the fabrication procedure see Section 3 of the Supporting Information. The final sample is shown in the scanning electron micrograph (SEM), consisting of square metasurfaces of $120 \times 120 \mu\text{m}$ size (Figure 2a). The SEMs shown in Figures 2b and c, demonstrate the high quality of the fabricated metasurfaces, matching closely to our design. Figure 2c shows a tilted-view SEM of the metasurface with nanodisks having straight sidewalls. Angle-resolved transmission measurements were performed on the metasurfaces, using an inverted optical microscope coupled to a spectrometer (Section 4, Supporting Information). The

angle-resolved transmission measurements, obtained using y -polarized incident light and a slit along the y -axis, are shown in Figures 2d, e. Figure 2d shows the transmission of the metasurface around the pump wavelength (730-970 nm) when illuminated at different incident angles (0° to $\pm 30^\circ$). The resonances of the metasurfaces are revealed by diagonal bands, several of them crossing at 0° (normal incidence). The resonance of interest, indicated by a white dotted circle, is centred around 865 nm, corresponding to λ_p . Similarly, Figure 2e shows the transmission of the metasurface around the signal wavelength (1400-1600 nm), as a function of the incident angle. In this case, the measurements indicate the excitation of a single resonance corresponding to the parabolic band. The parabolic shape denotes a blue-shift of the resonance, as the angle of incidence is increased from 0° to $\pm 30^\circ$. At normal incidence, the metasurface exhibits the excitation of a resonance centred around 1545 nm, indicated by a white dotted circle, and corresponding to λ_s . The linear response of the metasurface around the pump and signal wavelengths is symmetric with respect to the (positive and negative) angles of incidence, due to the symmetry of the metasurface along the y -axis. Angle-resolved transmission measurements using x -polarized incidence can be found in the Supporting Information, Figure S6. The transmission spectra corresponding to normal x - and y -polarized incidence are shown in Figures 2f and g. Figure 2f shows the resonant behavior of the metasurfaces around the pump wavelength λ_p (gray shaded region), for both incident polarizations. This resonance is slightly blue-shifted when using x -polarized incident light. **The resonance excited when using y -polarized incident light has a Q of ~ 173 . Figure 2g shows the excitation of a resonance around the signal wavelength λ_s (gray shaded region), only for y -polarized incident light, with an associated Q of ~ 103 .** The lower measured Q values, as compared to the calculated ones, are explained by imperfections on the fabricated metasurfaces. The fringes

observed in the transmission spectra (Figures 2e and g) are due to Fabry-Perot interferences in the sapphire substrate.

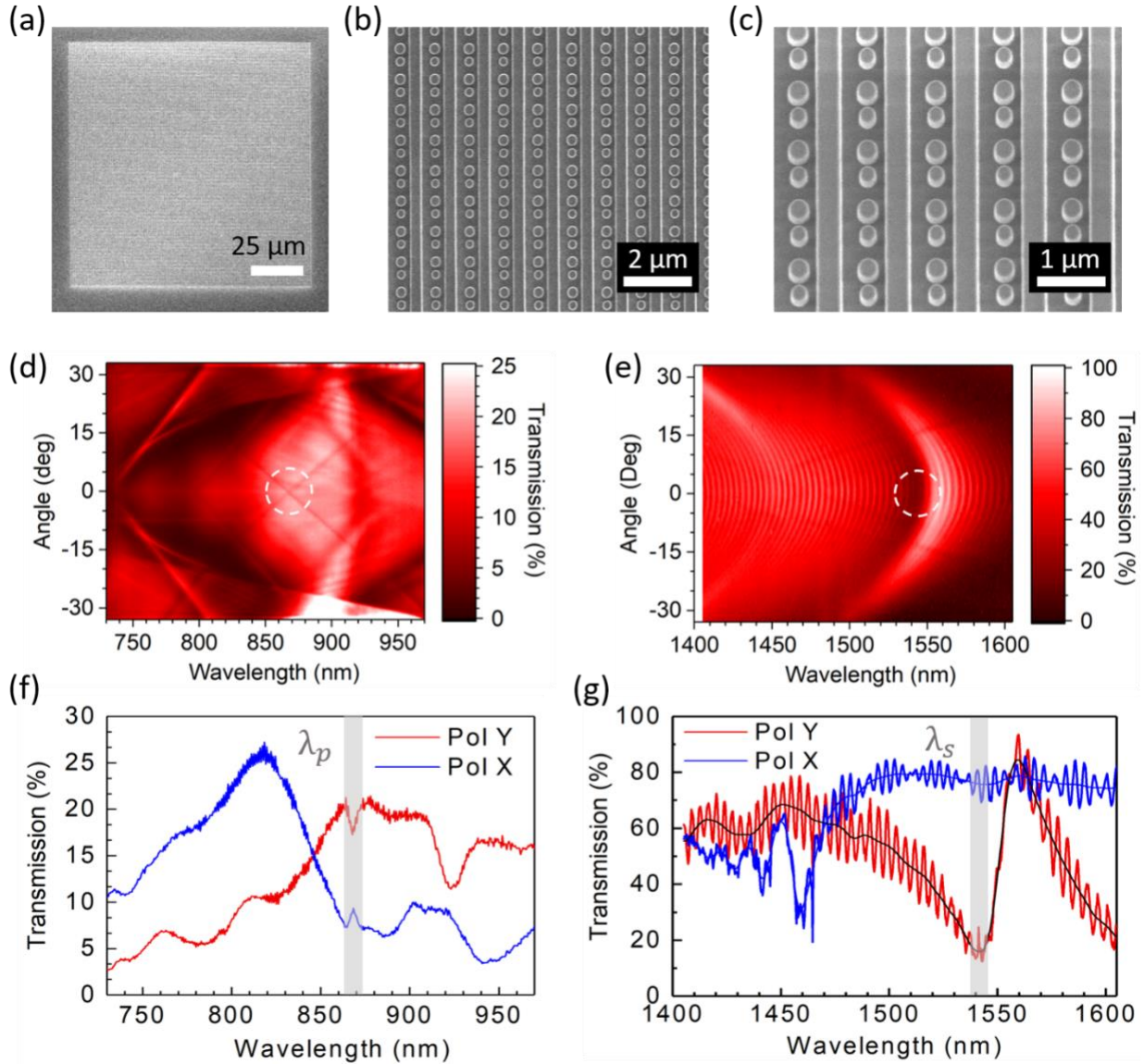


Figure 2. (a, b) Top-view and (c) tilted-view scanning electron micrographs (SEM) of fabricated crystalline GaP metasurfaces. Angle-resolved transmission spectra of metasurface measured around (d) the pump wavelength λ_p and (e) signal wavelength λ_s , under y -polarized incident light. Experimental transmission spectra of the metasurface measured around (f) the pump wavelength λ_p and (g) signal wavelength λ_s , under normal x - and y -polarized incident light. The transmission spectra in (f) and (g) exhibit two sharp resonances at λ_p and λ_s , indicated by gray vertical bars. Under y -polarized incident light, these resonances have an associated Q of (f) 173 and (g) 103.

Then, we measured the nonlinear response of the metasurface around the resonant wavelengths λ_p and λ_s , using the optical system described in Section 5 of the Supporting Information. First, we measured the SFG when varying the pump beam wavelength from 855 nm to 880 nm, in steps of 5 nm, while maintaining a fixed λ_s at 1545 nm. The spectra of the measured SFG are shown in Figure 3a, where maximum SFG enhancement is observed at the visible wavelength of 558 nm, corresponding to a pump beam at 875 nm. The use of longer pump wavelengths was, unfortunately, not accessible by our laser system. Next, we measured the SFG when varying the signal beam wavelength from 1525 nm to 1565 nm, while fixing λ_p at 875 nm. The measured spectra are shown in Figure 3b, where maximum SFG enhancement is observed at 558 nm, corresponding to a signal beam at 1545 nm. The maximum SFG enhancement shows good agreement with respect to λ_s resonance (Figure 2g) and is red shifted by ~ 10 nm with respect to λ_p resonance (Figure 2f). This red shift can be explained by a better mode matching of the SFG at a slightly longer pump wavelength.

Next, we measured the nonlinear emission of the metasurface when illuminated simultaneously by two beams with $\lambda_p = 875$ nm and $\lambda_s = 1545$ nm. In these measurements, an average power of 6 mW (1 mW) was used in the pump (signal) beam. The spectra obtained are shown in Figure 3c, where three nonlinear peaks are observed around the visible spectral range. The first two peaks, centered at 437 nm and 558 nm, correspond to the second harmonic of the pump beam ($\text{SHG}_{2\text{op}}$) and the SFG, respectively. The third peak, centered at 772 nm, corresponds to the second harmonic of the signal beam ($\text{SHG}_{2\text{os}}$). The band gap of the GaP semiconductor material is 2.26 eV, corresponding to a wavelength of ~ 550 nm, thus the extinction coefficient of GaP increases below this wavelength (gray line with squares, Figure 3c). Consequently, the $\text{SHG}_{2\text{op}}$ emission is partially absorbed by the material, explaining its lower intensity as compared to the SFG and $\text{SHG}_{2\text{os}}$. To corroborate

the origin of the spectral peak at 558 nm, the power of the incident beams was separately increased in steps of 1 mW. First, the average power of the signal beam (P_s) was increased from 7 to 15 mW, keeping constant the average power of the pump beam (P_p) at 10 mW. In every step, the SFG intensity was recorded, as shown in the top of Figure 3d. Similarly, the P_p was increased from 10 to 30 mW, keeping constant P_s at 15 mW, and the corresponding SFG intensity was recorded, as shown in the bottom of Figure 3d. The log-log plots in Figure 3d show a linear dependence of the SFG with the power of pump and signal beams. This linear dependence corroborates the spectral peak observed at 558 nm is generated by SFG, where both pump and signal beams contribute with a single photon to the nonlinear process (inset of Figure 3c). **Therefore, we have demonstrated the up-conversion of near-infrared light ($\lambda_s=1565$ nm) to the visible spectrum ($\lambda_{\text{SFG}}=558$ nm), through the use of a pump beam, within a metasurface. These results open up new opportunities for ultra-compact infrared imaging devices [40-42].**

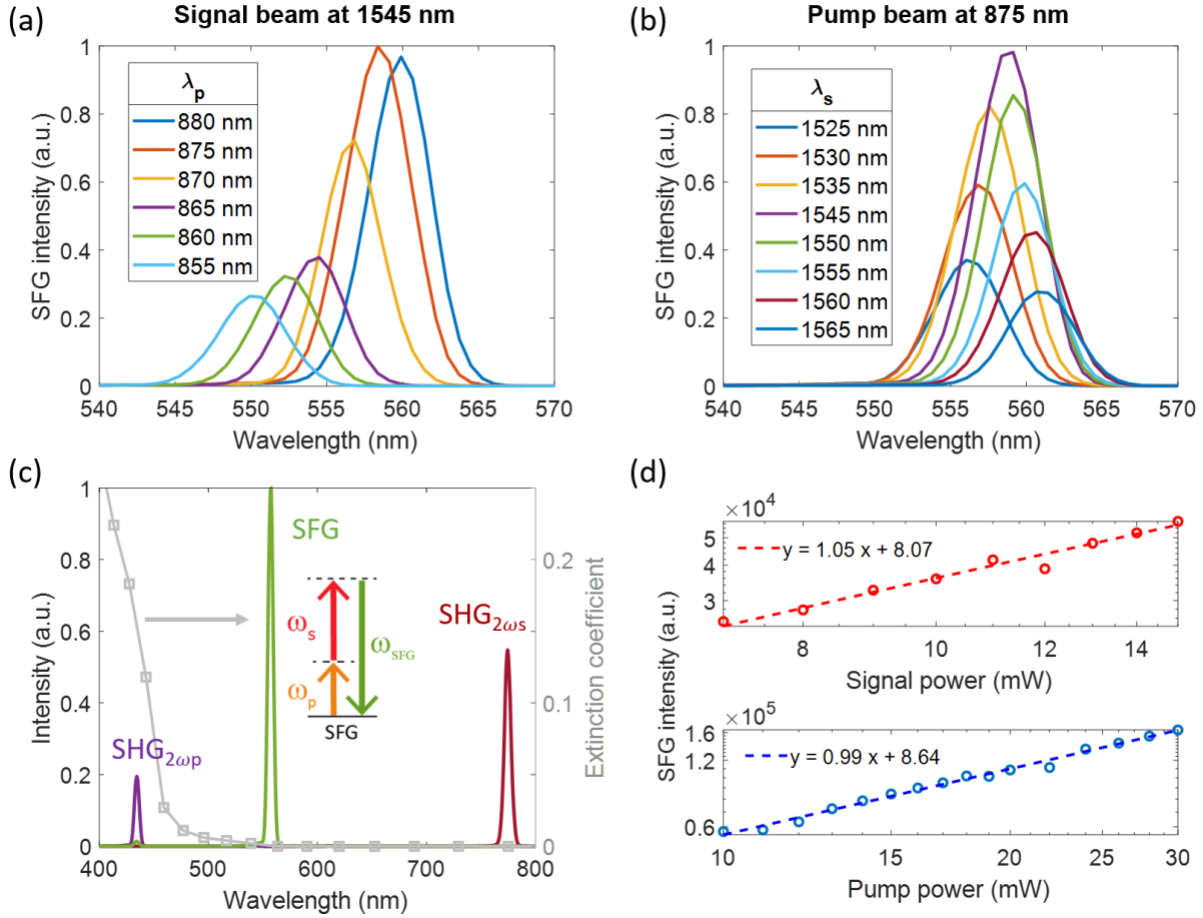


Figure 3. Spectral dependence of the SFG on the varying wavelength of (a) the pump beam from 855 to 880 nm, and (b) the signal beam from 1525 to 1565 nm. In the former case, the wavelength of the signal is fixed at 1545 nm, while in the latter case the wavelength of the pump is fixed at 875 nm. **In the spectra shown in (a) and (b) the pump and signal beams were set to the polarization states giving maximum nonlinear emission.** (c) Measured intensity of the three nonlinear emissions generated by metasurface (coloured lines), corresponding to SHG $_{2\omega_p}$, SFG and SHG $_{2\omega_s}$, and extinction coefficient of GaP semiconductor material (gray line with squares) as a function of wavelength. The energy level diagram corresponding to the SFG nonlinear process is shown in the inset. (d) SFG intensity as a function of average power in the pump beam (bottom) and signal beam (top). The experimental data, shown in a log-log plot, indicates a linear dependence of SFG with the power of pump and signal beams.

Next, we measured the dependence of the SFG emission with the polarization angle of the incident beams. In these measurements the wavelength of the incident beams are fixed to $\lambda_p = 875$ nm and $\lambda_s = 1545$ nm, where the maximum SFG emission is obtained. First, we rotate the pump beam polarization while maintaining a fixed the polarization along the y -axis in the signal beam. As

shown by the green curve in Figure 4a, maximum SFG emission is observed when the pump beam is polarized at $\sim 145^\circ$. Then, we rotate the signal beam polarization while maintaining a fixed polarization in the pump beam at 145° . In this case, maximum SFG emission is observed for a signal beam polarized along the y -axis, as shown by the green curve in Figure 4b. Therefore, the maximum SFG intensity is obtained for **non-parallel** polarization incidence of the excitation beams. **The pump polarization dependence of the SFG at neighboring resonant wavelengths observes a different behavior. These measurements can be found in Figure S7 of the Supporting Information.** In addition, we measured the polarization dependence of both generated second harmonics. In both cases, we observed maximum SHG for y -polarized incident beams, as shown by the purple and red curves in Figures 4a and b. These measurements agree with the corresponding calculations, shown in Figures 4c and d. The complex polarization dependence of the SFG can be explained by the nonlinear multipoles generated at the SFG wavelength (Supporting Information, Figure S5). In our metasurface, the scattering of light is mainly dominated by the nanodimers, while the nano-waveguides mainly dominate the trapping and confinement of light. Thus, in the nonlinear regime, the SFG emission is highly influenced by the scattering properties of the nanodimers. The nonlinearly generated multipoles from the nanodimers vary when rotating the pump polarization and their interferences lead to the unique SFG polarization dependence.

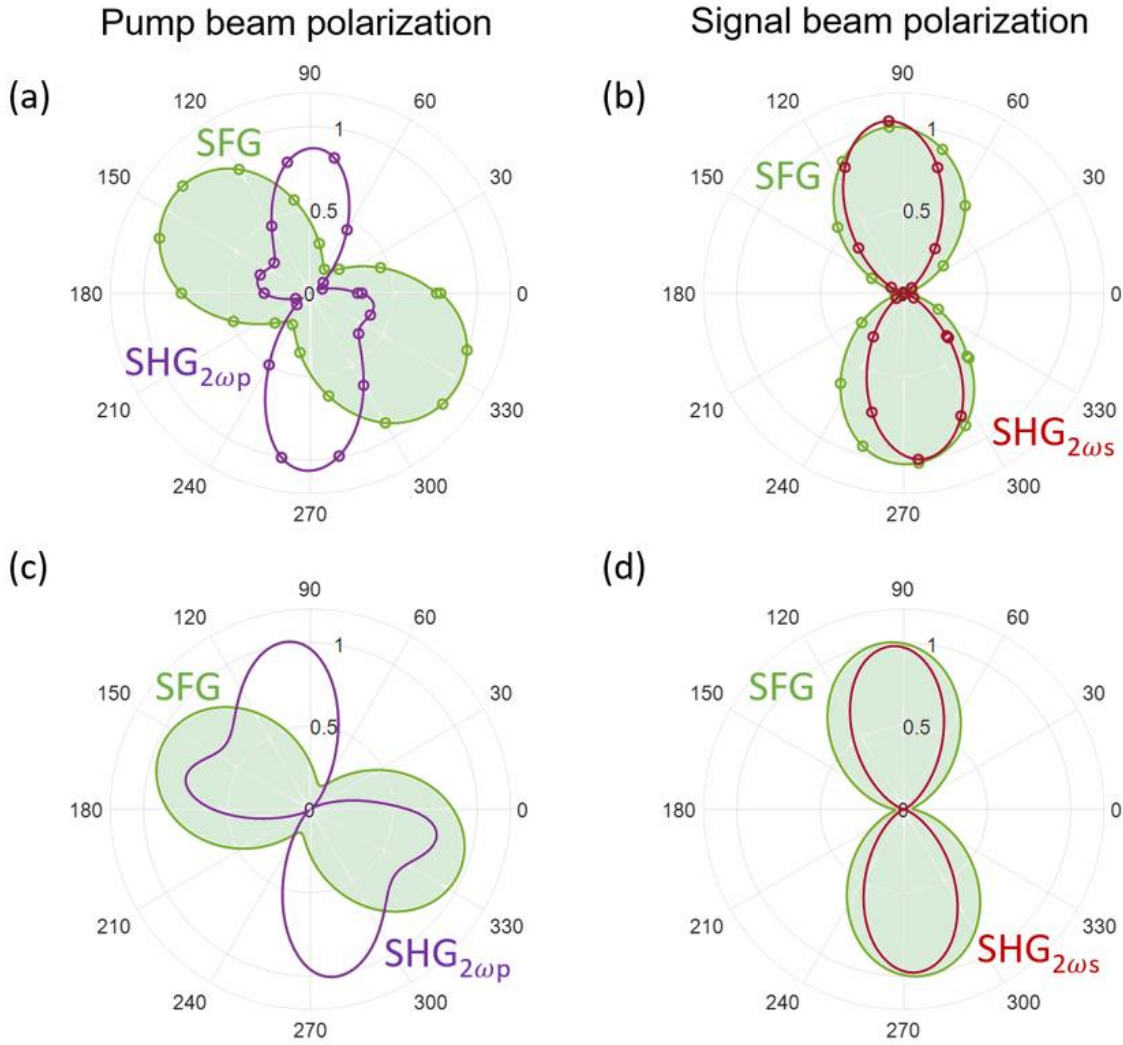


Figure 4. Polar plots showing the measured (a) pump polarization dependence of SFG and $\text{SHG}_{2\omega_p}$ and (b) signal polarization dependence of SFG and $\text{SHG}_{2\omega_s}$. The circles indicate experimental data, while the solid lines indicate the corresponding fittings. Calculated polar plots showing (c) the pump polarization dependence of SFG and $\text{SHG}_{2\omega_p}$ and (d) the signal polarization dependence of SFG and $\text{SHG}_{2\omega_s}$. The measured and calculated SFG intensity shown in (a) and (c) is obtained using a signal beam polarized along the y -axis. Meanwhile, the measured and calculated SFG intensity shown in (b) and (d) is obtained using a pump beam linearly polarized at 145° and 155° , respectively. These angles correspond to the configuration where maximum SFG is obtained. In these plots, 0° and 90° represent polarizations along the x - and y -axis, respectively. All nonlinear emissions are separately normalized.

The directionality of the nonlinear emissions was measured by performing back-focal plane (BFP) imaging (Section 6, Supporting information). Figure 5 shows the corresponding images, where the

nonlinear emission is captured as a function of the transverse momentum of the emitted photons, $k_{x,y} = 2\pi/\lambda \sin \vartheta_{x,y}$. Here, $\vartheta_{x,y}$ is the emission angle in x and y -directions. The measurement of $\vartheta_{x,y}$ is limited by the numerical aperture of the collecting objective (NA=0.9), to a maximum value of $\sim 64^\circ$ (white dashed circles in Figure 5). In every image, the input polarization of pump and signal beams is indicated by orange and red top-right arrows, respectively. In these measurements, the metasurface is illuminated from the substrate side, while the nonlinear emission is collected in a transmission geometry (air side). Figure 5a shows the SFG emitted by the metasurface at different input polarization of the pump beam (orange arrow), while maintaining the polarization of the signal beam fixed at 90° (red arrow). At an incident polarization of 20° in the pump beam (see left), the maximum SFG emission is directed to the (1,0) and (0,1) diffraction orders, as marked by the white squares in the plot. When the polarization of the incident pump beam is rotated to 60° (see center), the (0,0) diffraction order have similar intensity to the $(\pm 1,0)$, (0,1), and (1,1) diffraction orders. Finally, when the polarization of the incident pump beam is rotated to 100° (see right), the maximum intensity is observed at the (-1,0), (0,0) and (1,1) diffraction orders. In contrast, when the polarization of the signal beam is rotated, the intensity of all SFG diffraction orders follow the same trend, going from a maximum to a minimum intensity at the same time (see video in the Supporting Information). This behavior indicates the intensity of the SFG diffraction orders can be independently controlled by rotating the pump beam polarization. **The observed control over the diffraction orders carrying maximum emission can be explained by the coupling of the pump field into the nonlinear polarization currents - based on the nonlinear tensor of the GaP semiconductor material (Figure S4, Supporting Information). In addition, the nonlinear multipolar generation and their superposition can also induce the observed control over the emission of the nonlinear diffraction orders [10, 43]. Intensity plot profiles of the SFG diffraction**

orders are shown in Figure 5b, corresponding to the BFP images in Figure 5a. Specifically, these intensity profiles were obtained from horizontal cross sections performed in the middle of the images, as shown in the inset of Figure 5b (see left). The SFG diffraction orders with normalized intensity above 0.8 (see gray shaded areas) are the ones highlighted in Figure 5a by white squares. In our case, the intensity variations among the $(-1,0)$, $(0,0)$ and $(1,0)$ diffraction orders can be as large as $\sim 50\%$. The control and variation over the intensity of nonlinear diffraction orders have potential applications for wavefront manipulation [44].

Figure 5c shows the BFP images of the three nonlinear emissions generated by the metasurface. The three nonlinearly generated waves exhibit normal emission (zero-order diffraction), and the diffraction of higher orders as the wavelength of the nonlinear emission decreases. In every case, the input polarization of the incident beam(s) was set to the one(s) generating maximum nonlinear intensity (Figure 4). In Figure 5b, larger emission angles are observed along the y -direction as compared to the x -direction, corresponding to the smaller periodicity of the metasurface along the y -direction. In this case, maximum SFG intensity (see center) is observed in the $(1,0)$, $(0,0)$ and $(0,1)$ diffraction orders. In addition to the forward SFG observed in Figure 5, the metasurface also generates backward SFG. A portion of the backward SFG is trapped inside the glass substrate (SFG inset of Figure 5b) due to total internal reflection produced at the substrate-air interface (Section 6, Supporting Information).

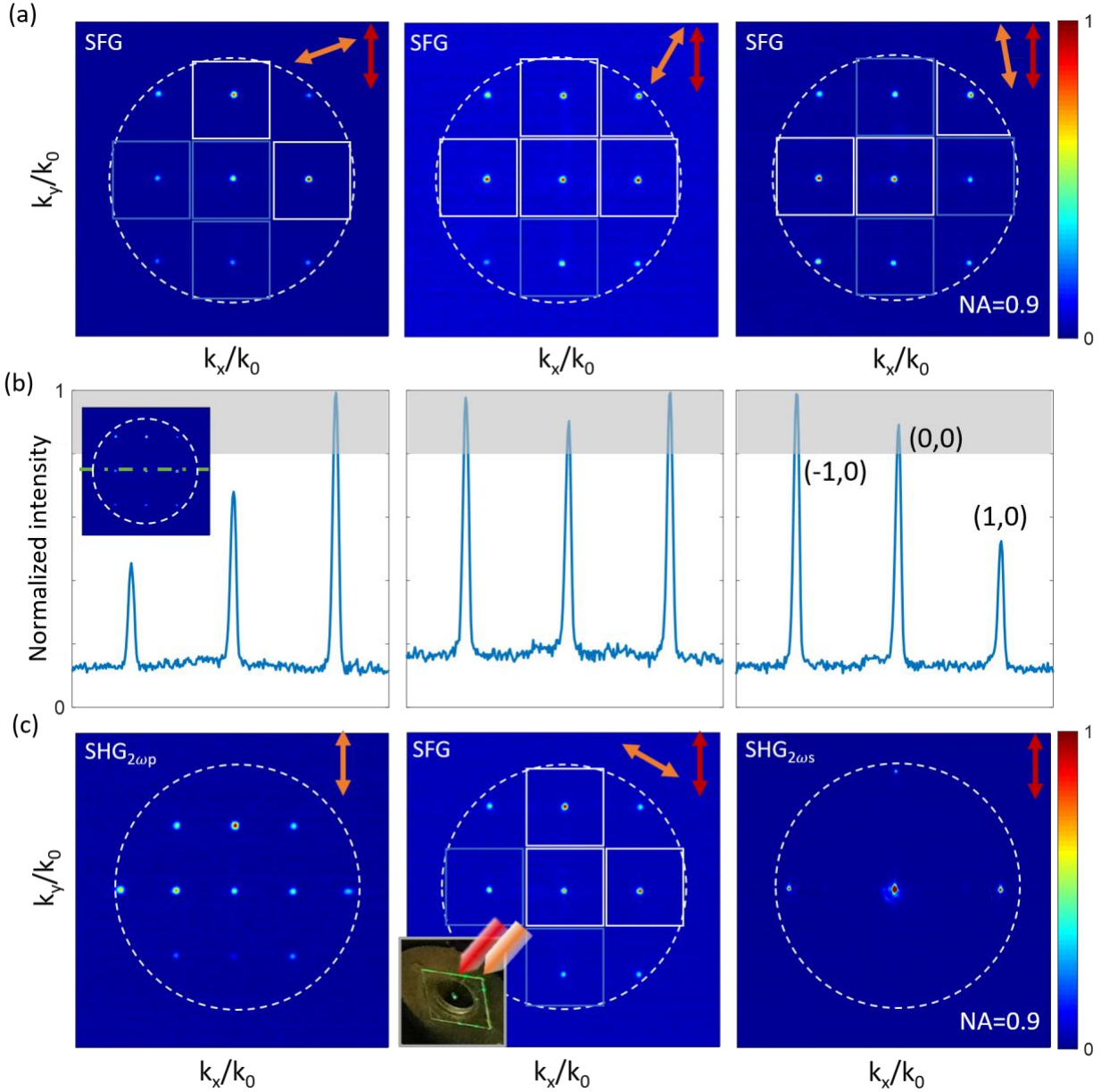


Figure 5. (a,c) Fourier plane images of nonlinear emissions generated by the GaP metasurface when illuminated by different polarization angles of the excitation beams. The orange and red upper-right arrows indicate the incident polarization of the pump and signal beams, respectively. The dashed white circle indicates the maximum angular field of view due to the numerical aperture of the collecting objective lens (NA=0.9). The squares delimit the different SFG diffraction orders, and the white ones highlight the SFG diffraction orders of high intensity. The intensities of the images are not comparable to each other since they were normalized separately. (a) Fourier plane images of the SFG measured when the incident signal beam is polarized at 90° and the incident pump beam is polarized at 20° (left), 60° (center) and 100° (right). (b) Intensity plot profiles corresponding to horizontal cross sections (see left inset) performed in the middle of (a) Fourier plane images. The gray shaded areas indicate the diffraction orders with normalized intensities above 0.8. (c) Fourier plane images of SHG_{2 ω _p}, SFG and SHG_{2 ω _s} emissions. A photo of the SFG

emission is shown in the inset, where the red and orange arrows indicate the direction of the incident beams.

Finally, the forward SFG power was measured and a conversion efficiency of 2.5×10^{-4} [W^{-1}] was obtained, using a low signal beam intensity of 12.5 MW/cm^2 and a pump beam intensity of 137 MW/cm^2 (Section 7, Supporting Information). Here, the forward SFG corresponds to the total power emitted from the six collected diffraction orders (Figure 5). This efficiency is 100 times higher than the SFG reported in Mie-type resonant metasurfaces [42] and is the highest SFG efficiency reported to date. The high efficiency indicates the trifactor importance of the material's transparency, its near-field confinement due to the high-Q BIC resonances, and mode matching due to the waveguide type geometry of the metasurface.

In summary, we have demonstrated highly efficient sum-frequency generation in GaP high-Q metasurfaces. Our metasurface design supports double waveguide-type BIC resonances, thereby when the metasurface is simultaneously illuminated by a pump beam at 875 nm and a signal beam at 1545 nm it generates efficient SFG. A normalized conversion efficiency of 2.5×10^{-4} [W^{-1}] was measured by analysing the emission into forward diffraction orders. In stark contrast to harmonic generation processes, in the SFG process, the maximum efficiency is obtained for **non-parallel** polarization states of the two input beams. The observed non-trivial polarization dependence of the SFG allows for independent control and encoding of the diffraction orders carrying maximum emission. Our results open new opportunities for infrared to visible up-conversion and light sources.

ASSOCIATED CONTENT

Supporting Information

The Supporting information is available free of charge.

AUTHOR INFORMATION

Corresponding Author

* E-mail: rocio.camacho@anu.edu.au

** **Current affiliation:** FZU-Jinjiang Joint Institute of Microelectronics, Fuzhou University, Jinjiang, China, 362200;

ACKNOWLEDGMENT

The work was supported by the Australian Research Council under Centres of Excellence (CE200100010) and Discovery programs (DP190101559). This work was also supported by the Quantum Technologies for Engineering (QTE) program of A*STAR (A1685b0005) and MTC Programmatic Grant No. M21J9b0085 (Singapore). M.R. and L.X. acknowledges support from the UK Research and Innovation Future Leaders Fellowship (MR/T040513/1).

REFERENCES

1. Grinblat, G., *Nonlinear Dielectric Nanoantennas and Metasurfaces: Frequency Conversion and Wavefront Control*. ACS Photonics, 2021. **8**(12): p. 3406-3432.
2. Krasnok, A., M. Tymchenko, and A. Alù, *Nonlinear metasurfaces: a paradigm shift in nonlinear optics*. Materials Today, 2018. **21**(1): p. 8-21.
3. Liu, S., et al., *Resonantly Enhanced Second-Harmonic Generation Using III-V Semiconductor All-Dielectric Metasurfaces*. Nano Lett, 2016. **16**(9): p. 5426-32.
4. Löchner, F.J.F., et al., *Polarization-Dependent Second Harmonic Diffraction from Resonant GaAs Metasurfaces*. ACS Photonics, 2018. **5**(5): p. 1786-1793.
5. Marino, G., et al., *Zero-Order Second Harmonic Generation from AlGaAs-on-Insulator Metasurfaces*. ACS Photonics, 2019. **6**(5): p. 1226-1231.
6. Gigli, C., et al., *Polarization- and diffraction-controlled second-harmonic generation from semiconductor metasurfaces*. Journal of the Optical Society of America B, 2019. **36**(7).
7. Gao, Y., et al., *Nonlinear Holographic All-Dielectric Metasurfaces*. Nano Lett, 2018. **18**(12): p. 8054-8061.
8. Shcherbakov, M.R., et al., *Enhanced third-harmonic generation in silicon nanoparticles driven by magnetic response*. Nano Lett, 2014. **14**(11): p. 6488-92.

9. Wang, L., et al., *Nonlinear Wavefront Control with All-Dielectric Metasurfaces*. Nano Lett, 2018. **18**(6): p. 3978-3984.
10. Andrea, T., et al., *Third-harmonic light polarization control in magnetically resonant silicon metasurfaces*. Opt. Express, 2021. **29**(8): p. 11605--11612.
11. Semmlinger, M., et al., *Vacuum Ultraviolet Light-Generating Metasurface*. Nano Letters, 2018. **18**(9): p. 5738-5743.
12. Semmlinger, M., et al., *Generating Third Harmonic Vacuum Ultraviolet Light with a TiO₂ Metasurface*. Nano Letters, 2019. **19**(12): p. 8972-8978.
13. Zubyuk, V.V., et al., *Externally Driven Nonlinear Time-Variant Metasurfaces*. ACS Photonics, 2022. **9**(2): p. 493-502.
14. Boyd, R.W., *Nonlinear optics*. 2020: Academic press.
15. Rahmani, M., et al., *Nonlinear frequency conversion in optical nanoantennas and metasurfaces: materials evolution and fabrication*. Opto-Electronic Advances, 2018. **1**(10): p. 180021-1-180021-12.
16. Cambiasso, J., et al., *Bridging the Gap between Dielectric Nanophotonics and the Visible Regime with Effectively Lossless Gallium Phosphide Antennas*. Nano Letters, 2017. **17**(2): p. 1219-1225.
17. Wilson, D.J., et al., *Integrated gallium phosphide nonlinear photonics*. Nature Photonics, 2020. **14**(1): p. 57-62.
18. Anthur, A.P., et al., *Continuous wave second harmonic generation enabled by quasi-bound-states in the continuum on gallium phosphide metasurfaces*. Nano Letters, 2020. **20**(12): p. 8745-8751.
19. Shcherbakov, M.R., et al., *Generation of even and odd high harmonics in resonant metasurfaces using single and multiple ultra-intense laser pulses*. Nature communications, 2021. **12**(1): p. 1-6.
20. Liu, S., et al., *An all-dielectric metasurface as a broadband optical frequency mixer*. Nature communications, 2018. **9**(1): p. 1-6.
21. Gianni, Q.M., et al., *Engineering gallium phosphide nanostructures for efficient nonlinear photonics and enhanced spectroscopies*. Nanophotonics, 2021. **10**(17): p. 4261--4271.
22. Yuan, Q., et al., *Second Harmonic and Sum-Frequency Generations from a Silicon Metasurface Integrated with a Two-Dimensional Material*. ACS Photonics, 2019. **6**(9): p. 2252-2259.
23. Blechman, Y., et al., *Optimizing the Nonlinear Optical Response of Plasmonic Metasurfaces*. Nano Letters, 2019. **19**(1): p. 261-268.
24. Jay, E.S., et al., *Optical parametric oscillator based on four-wave mixing in microstructure fiber*. Opt. Lett., 2002. **27**(19): p. 1675--1677.
25. Fulconis, J., et al., *Nonclassical Interference and Entanglement Generation Using a Photonic Crystal Fiber Pair Photon Source*. Physical Review Letters, 2007. **99**(12): p. 120501.
26. Liu, Y., et al., *Difference-Frequency Generation in Polaritonic Intersubband Nonlinear Metasurfaces*. Advanced Optical Materials, 2018. **6**(20): p. 1800681.
27. von Neumann, J. and E.P. Wigner, *Über das Verhalten von Eigenwerten bei adiabatischen Prozessen*, in *The Collected Works of Eugene Paul Wigner*. 1993, Springer. p. 294-297.
28. Koshelev, K., et al., *Nonlinear metasurfaces governed by bound states in the continuum*. ACS Photonics, 2019. **6**(7): p. 1639-1644.

29. Liu, Z., et al., *High-Q Quasibound States in the Continuum for Nonlinear Metasurfaces*. Phys Rev Lett, 2019. **123**(25): p. 253901.
30. Xu, L., et al., *Dynamic Nonlinear Image Tuning through Magnetic Dipole Quasi-BIC Ultrathin Resonators*. Adv Sci (Weinh), 2019. **6**(15): p. 1802119.
31. Cizhe, F., et al., *High-Q resonances governed by the quasi-bound states in the continuum in all-dielectric metasurfaces*. Opto-Electronic Advances, 2021. **4**(6): p. 200030-1-200030-10.
32. Suhara, T. and H. Nishihara, *Theoretical analysis of waveguide second-harmonic generation phase matched with uniform and chirped gratings*. IEEE Journal of Quantum Electronics, 1990. **26**(7): p. 1265-1276.
33. Mondia, J.P., et al., *Enhanced second-harmonic generation from planar photonic crystals*. Optics Letters, 2003. **28**(24): p. 2500-2502.
34. Centeno, E., D. Felbacq, and D. Cassagne, *All-Angle Phase Matching Condition and Backward Second-Harmonic Localization in Nonlinear Photonic Crystals*. Physical Review Letters, 2007. **98**(26): p. 263903.
35. Ning, T., et al., *Efficient second-harmonic generation in silicon nitride resonant waveguide gratings*. Optics Letters, 2012. **37**(20): p. 4269-4271.
36. Joannopoulos, J.D., et al., *Photonic Crystals: Molding the Flow of Light - Second Edition*. 2011: Princeton University Press.
37. Huang, L., et al., *Atomically Thin MoS₂ Narrowband and Broadband Light Superabsorbers*. ACS Nano, 2016. **10**(8): p. 7493-7499.
38. Huang, L., et al., *Pushing the limit of high-Q mode of a single dielectric nanocavity*. Advanced Photonics, 2021. **3**(1): p. 016004.
39. Huang, L., Y. Yu, and L. Cao, *General Modal Properties of Optical Resonances in Subwavelength Nonspherical Dielectric Structures*. Nano Letters, 2013. **13**(8): p. 3559-3565.
40. Demur, R., et al., *Near-infrared to visible upconversion imaging using a broadband pump laser*. Optics Express, 2018. **26**(10): p. 13252-13263.
41. Chen, Y., et al., *Frequency up-conversion of an infrared image via a flat-top pump beam*. Optics Communications, 2020. **460**: p. 125143.
42. Camacho-Morales, R., et al., *Infrared upconversion imaging in nonlinear metasurfaces*. Advanced Photonics, 2021. **3**(3): p. 036002.
43. Balanis, C.A., *Antenna theory: analysis and design*. 2005: Wiley-Interscience.
44. Liu, B., et al., *Nonlinear Wavefront Control by Geometric-Phase Dielectric Metasurfaces: Influence of Mode Field and Rotational Symmetry*. Advanced Optical Materials, 2020. **8**(9): p. 1902050.